# Catalysis Science & Technology



PAPER

View Article Online
View Journal | View Issue



Cite this: Catal. Sci. Technol., 2021, 11, 5109

# decomposition using alkaline earth metal-based perovskites† Fnu Gorky, Da Jolie M. Lucero, Db James M. Crawford, Db Beth A. Blake, a

Insights on cold plasma ammonia synthesis and

Fnu Gorky, <sup>1</sup> Jolie M. Lucero, <sup>1</sup> James M. Crawford, <sup>1</sup> Beth A. Blake, <sup>a</sup> Shelby R. Guthrie, <sup>a</sup> Moises A. Carreon <sup>1</sup> and Maria L. Carreon <sup>1</sup> \*

The synergistic combination of solid catalysts and plasma for the synthesis of ammonia has recently attracted considerable scientific interest. Herein, we explore MgTiO<sub>3</sub>, CaTiO<sub>3</sub>, SrTiO<sub>3</sub>, and BaTiO<sub>3</sub> perovskites as effective catalysts for the synthesis and decomposition of ammonia via cold plasma. MgTiO<sub>3</sub> perovskite, which contains the most electronegative alkaline metal of all the studied perovskites, resulted in the highest ammonia synthesis rate with a value of 12.16  $\mu$ mol min<sup>-1</sup> m<sup>-2</sup>, which is around 50 times the value of only plasma, 0.24 µmol min<sup>-1</sup>. The high electronegativity of Mg can be assisting the dissociation of the triple nitrogen covalent bond. This intrinsic property of Mg perovskite added to the homogeneity of the plasma arising from the dielectric constant value of this perovskite might be synergistically responsible for the high ammonia synthesis rate observed. Interestingly, ammonia production over MgTiO<sub>3</sub> perovskite is almost double the performance of traditional oxides and some microporous crystals. We also explored the ammonia decomposition reaction due to the possibility of the importance of the reversible reaction owing to the electron collision with the ammonia molecules formed. Ammonia decomposition increased as plasma power increased. This points out the benefit of running at low plasma power and the need to design plasma reactors where the newly formed ammonia molecules can be removed from the reaction system to avoid further electron collision. The highest ammonia decomposition yield was 44.37% at 20 W corresponding to an energy yield of 5.06 g-NH<sub>3</sub> kW h<sup>-1</sup>.

Received 23rd April 2021, Accepted 8th June 2021

DOI: 10.1039/d1cy00729g

rsc.li/catalysis

# Introduction

Ammonia is an essential chemical for food security due to its use in fertilizers. Ammonia synthesis is currently performed at industrial scale through the Haber–Bosch (HB) process, which typically occurs at energy-intensive conditions of temperature and pressure ( $\sim 500$  °C and 500 bar). In fact, it is considered the most energy-consuming process in the chemical industry. Global ammonia production for 2018 was  $\sim 249.4$  million tons, consuming 1–2% of the world's energy, using 2–3% of the world's natural gas output, and emitting over 300 million metric tons of  $\rm CO_2$ . With such energy condition requirements, the HB process is only economically viable at large-scale plants that demand huge capital investments and access to continuous electric power to keep

Based on the above, the development of simplified alternatives to the HB process at milder conditions and compatible with intermittent electric power (e.g. from renewable energy sources) is a critical step toward small-scale, decentralized ammonia production. However, the implementation of this technology to fully replace fossil fuels for electricity, heat and transportation will be only feasible until there is an effective energy storage and distribution technology. Based on this premise, herein we employ non-thermal plasma catalysis as an alternative and transformative process that leverages renewable electricity to produce ammonia with high selectivity.

Plasma catalysis is highly appealing as an alternative route to activate the "source gas" by collision with electrons. This can be exploited to help activate strong bonds (e.g. C–H bond in CH<sub>4</sub> and N $\equiv$ N bond in N<sub>2</sub>). Initial forays<sup>8</sup> have indicated the potential of plasma to facilitate catalysis under mild conditions. However, optimizing catalysts for plasma-assisted reactions is challenging due to the high complexity of plasmas and plasma-catalyst interactions. The latter are

the process continuously running.<sup>4,5</sup> Consequently, ammonia synthesis is currently highly centralized, hampering the access of farms in remote areas to affordable fertilizers.<sup>6</sup>

<sup>&</sup>lt;sup>a</sup> Chemical and Biological Engineering Department, South Dakota School of Mines & Technology, 501 E Saint Joseph St, Rapid City, South Dakota–57701, USA. E-mail: Maria.CarreonGarciduenas@sdsmt.edu

<sup>&</sup>lt;sup>b</sup> Chemical and Biological Engineering Department, Colorado School of Mines, Golden. CO 8040. USA

 $<sup>\</sup>dagger$  Electronic supplementary information (ESI) available. See DOI: 10.1039/d1cy00729g

not well understood but are known to engender synergy, 12 i.e. higher performance (e.g. better conversion or selectivity) than the sum of the individual performances of the plasma and the catalyst when choosing a suitable plasma-catalyst pair. 13,14 Considerable research using metal-based catalysts<sup>15–19</sup> and different plasma regimens including vacuum<sup>20-23</sup> and atmospheric conditions<sup>24-26</sup> has been documented. However, a major challenge is still the rational tailoring of a catalyst that can exploit the benefits of the plasma surroundings. The development of superior performance catalysts for plasma-assisted ammonia synthesis requires novel robust materials tailored specifically for plasma.

Perovskites are potentially suitable and appealing materials for plasma catalysis. Perovskites are synthetic compounds that have an orthorhombic crystal structure identical to that of the naturally occurring mineral with the same name and that share a structurally similar chemical formula. The typical molecular composition of perovskites is ABX3, where A and B represent metal ions (A is usually larger than B) and X is oxygen. In their crystal structure, B and X form a BX<sub>6</sub> octahedron, where B lies in the center and X locates at the vertex of the octahedron. The BX6 octahedrons link each other, forming a network structure in threedimensional space by sharing the same X corners.<sup>27</sup> These materials form a polar unit cell due to the distorted dimensional structure inside the bulk.<sup>28</sup> This polar unit cell can generate a spontaneous and permanent electric polarization in the presence of an external electric field.<sup>29-31</sup> Deformation caused by cationic substitution can further tune these properties such as phase stability by strain relaxation.<sup>32</sup> Moreover, a ferroelectric phase can transform into a nonferroelectric phase when the temperature exceeds a particular value. This phase transformation temperature is called Curie temperature  $(T_c)$ .<sup>30</sup> Above  $T_c$ , the crystal structure of ABX<sub>3</sub> perovskites transforms to a cubic structure with minimal polarization, which is defined as the paraelectric phase.<sup>33</sup> Perovskites have emerged as one of the most promising and efficient low-cost energy materials for various optoelectronic and photonic device applications as well as robust catalysts. The unique physical properties of perovskite materials such as high-absorption coefficient, long-range ambipolar charge transport, low exciton-binding energy, high dielectric constant, ferroelectric properties, etc. make them highly attractive for such applications. Perovskite-type catalysts have been evaluated for plasma VOC removal34 due to their enhanced stability and activity. Furthermore, it has been documented that the discharge could be effectively enhanced by introducing a perovskite-type catalyst due to the high dielectric constant.35,36 Most of the existing plasma research on porous materials conclude on the potential benefits such as the formation of microdischarges, 37-41 short-lived species inside the pores, 37,38 and increase of the lifetime of the latter species in the pores, making them available for subsequent surface reactions.<sup>39</sup> Apart from the advantages mentioned above, perovskites are appealing materials for ammonia

synthesis due to their (1) high dielectric constants that might benefit the plasma homogeneity which has been identified as a key challenge in the plasma field; (2) readiness to dissolve hydrogen<sup>42,43</sup> (this property can be modified with the chemistry of the perovskite); (3) weak bonding with nitrogen;44 (4) high chemical stability in the presence of water and some hydrocarbons, which are typical impurities in natural gas wells (hydrogen for ammonia production is typically obtained from steam reforming of methane<sup>45</sup>); (5) their low acidity (specially for alkaline earth titanates) which has been pointed out to be beneficial for both thermal<sup>46</sup> and plasma catalytic synthesis of ammonia; 26,47 and (6) the presence of a functional porous crystalline structure. This set of unique features make perovskites highly attractive phases for the synthesis of ammonia via plasma.

Herein, we demonstrate that MgTiO<sub>3</sub>, CaTiO<sub>3</sub>, SrTiO<sub>3</sub>, and BaTiO<sub>3</sub> perovskites exhibited enhanced catalytic performance for the synthesis and decomposition of ammonia assisted via cold plasma.

Fig. 1 shows the general structure of the perovskites employed in this work: (a) MgTiO<sub>3</sub> (hexagonal), <sup>48</sup> (b) CaTiO<sub>3</sub> (orthorhombic),<sup>49</sup> (c) SrTiO<sub>3</sub> (cubic)<sup>50</sup> and (d) BaTiO<sub>3</sub> (cubic).51

# Results and discussion

### Plasma catalytic ammonia synthesis using alkaline-earth metal perovskites

To test our central hypothesis on the potential of perovskites as effective catalysts for plasma catalytic ammonia synthesis, we evaluated the catalytic performance on a dielectric barrier discharge (DBD) reactor for four commercially available perovskites: MgTiO<sub>3</sub>, CaTiO<sub>3</sub>, SrTiO<sub>3</sub> and BaTiO<sub>3</sub> (perovskites containing alkaline earth metals). The results are summarized in Fig. 2. The experiments were carried out at a total flow rate of 25 sccm and different feed flow ratios ranging from 1:6 to 3:1 ratio of nitrogen to hydrogen (N2: H<sub>2</sub>). Interestingly, at the best performance ratio, i.e., 1:1 ratio, MgTiO3 surpasses the catalytic performance of the rest of the perovskites. Fig. 2 also shows the impact of the plasma-activated gas phase on the synthesis rate, since the ammonia production is affected by the available species present to interact with the perovskite catalyst. The performance of the four perovskites containing alkaline earth metals at 1:1 ratio can be seen in Fig. 2b. The value for only plasma in Fig. 2b is expressed in μmol min<sup>-1</sup>. For the plasma only reaction, there is no catalyst packed in the cross section of the DBD. When there is no packed perovskite in the cross section of the reactor the W electrode is in there anyway. In this case, W was selected due to its inertness for plasma catalytic ammonia synthesis. The reaction in this case is taking place in the gas phase, the walls of the reactor and possibly on the electrode<sup>21</sup> (surface area of  $8.07 \times 10^{-5}$  m<sup>2</sup>). Our previous experimental modelling work suggests that when a catalyst is packed in the reactor, the effect of the surface area of the catalyst

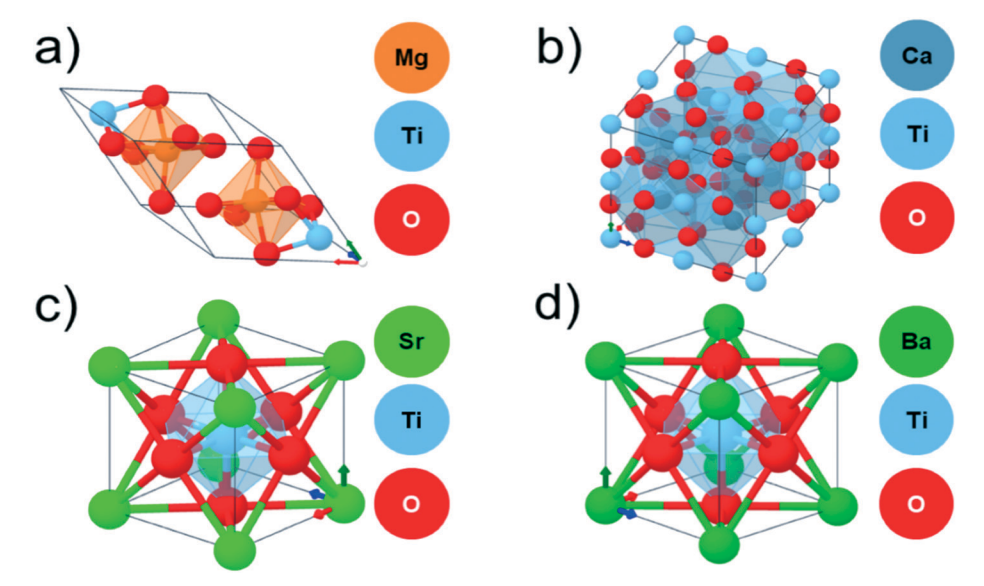


Fig. 1 General structure of the different perovskites employed in this study: (a) MgTiO<sub>3</sub> (hexagonal), (b) CaTiO<sub>3</sub> (orthorhombic), (c) SrTiO<sub>3</sub> (cubic) and (d) BaTiO<sub>3</sub> (cubic).

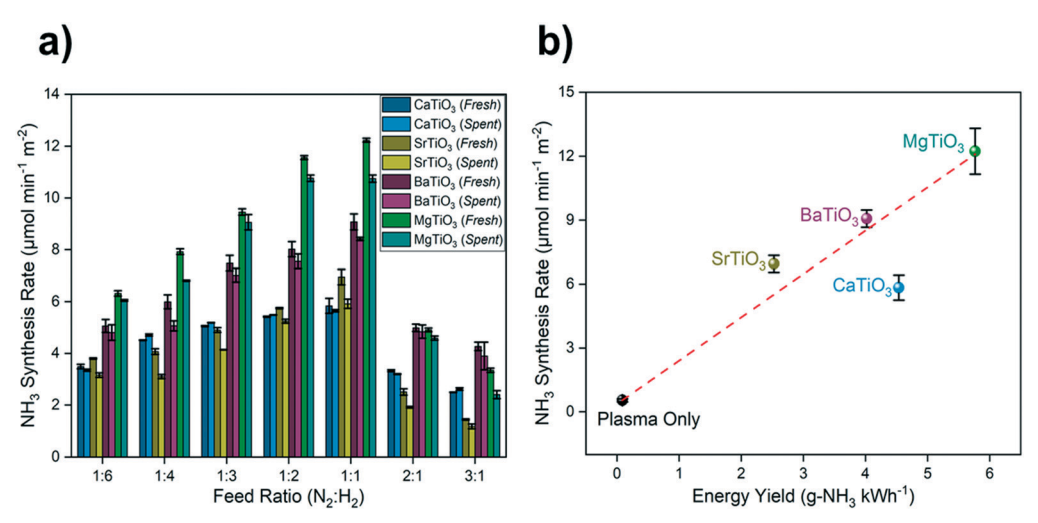


Fig. 2 (a) Ammonia synthesis rate as a function of feed flow ratio for the studied perovskites, (b) ammonia synthesis rate for different alkaline earth metal perovskites at a 1:1 flow ratio and total flow rate of 25 sccm.

overcomes the others including the reactor wall effect.<sup>21</sup> Moreover, the type of discharge when having only an electrode compared to when there is a porous material packed in the cross section transitions from filamentary to microdischarge. All this makes a straight comparison based on the surface area challenging.

The catalytic activity shown by the perovskites was in the order (MgTiO<sub>3</sub> (12.24  $\mu$ mol min<sup>-1</sup> m<sup>-2</sup>) > BaTiO<sub>3</sub> (9.07  $\mu$ mol  $min^{-1} m^{-2}$ ) > SrTiO<sub>3</sub> (6.95 µmol  $min^{-1} m^{-2}$ ) > CaTiO<sub>3</sub> (5.84 μmol min<sup>-1</sup> m<sup>-2</sup>)), which is in good agreement with the highest electronegativity alkaline-earth metal element within the perovskites to perform best:  $(Mg (1.31) > CaTiO_3 (1.00) >$ Sr(0.95) > Ba(0.89)). These values are on the Pauling scale which is unitless. It can be observed that Mg exhibits the highest electronegativity value as compared to the other metals. Therefore, a plausible explanation for MgTiO<sub>3</sub> perovskite performing better than the other perovskites is that it can weaken the triple covalent nitrogen bond, hence acting synergistically with the external electron excitation provided by the plasma to help with the nitrogen triple bond dissociation. Moreover, previous reports on both thermal and plasma catalysis have demonstrated the use of Mg-based catalysts for ammonia synthesis (see state-of-the-art table in the ESI† file, Table S1). As can be observed in Table S1,† Mgbased catalysts show an ammonia synthesis rate ranging from 3 µmol min<sup>-1</sup> m<sup>-2</sup> to 32 µmol min<sup>-1</sup> m<sup>-2</sup> for the case of thermal catalysis, while for plasma catalytic ammonia synthesis with Mg-based catalysts in a DBD, the ammonia synthesis rates are higher and range from 36.1 µmol min<sup>-1</sup> m<sup>-2</sup> to 73.4 μmol min<sup>-1</sup> m<sup>-2</sup>. A direct comparison cannot be

done due to the type of reactor, reaction conditions and different thermal and plasma reaction pathways. However, an apparent synergistic effect of Mg with plasma seems to lead to higher ammonia production. Here in, optical emission spectroscopy (OES) analysis shows experimentally the synergistic effect of plasma + MgTiO<sub>3</sub>. In this analysis, the pivotal nitrogen excited species show higher intensities when employing plasma and the perovskite as compared to only plasma (Fig. S1†). Recyclability is a key feature of any catalyst intended for potential commercial application. Based on this, we performed 3 cycles for MgTiO<sub>3</sub>. MgTiO<sub>3</sub> was shown to be a robust catalyst with the first cycle synthesis rate value of 13.06  $\pm$  0.34  $\mu$ mol min<sup>-1</sup> m<sup>-2</sup> and 3rd cycle value of 11.08  $\pm$ 0.84 μmol min<sup>-1</sup> m<sup>-2</sup> which results in only ~15% catalytic decay (Fig. S2†). Moreover, from the surface area analysis we can observe minimal losses in surface area after plasma exposure. The largest loss in surface area was noted in CaTiO<sub>3</sub> (ca. 10%) followed by MgTiO<sub>3</sub> (ca. 6%). BaTiO<sub>3</sub> and SrTiO<sub>3</sub> showed no appreciable loss in surface area after use.

Of all of the previously mentioned advantages of perovskites, the only property that we found to have an evident correlation with catalytic performance was the dielectric constant. Nevertheless, the other properties can be potentially beneficial for plasma catalysis. For instance, porous crystalline structures have been shown to be beneficial as catalysts for ammonia plasma synthesis (see ref. 23, 24 and 53). The effect of hydrogen recombination<sup>21</sup> as postulated by our group has been found to be important in this work since a limited presence of hydrogen results in higher ammonia production.

#### The effect of plasma on the tested perovskites

Fig. 3 shows the powder X-ray diffraction patterns of the fresh and spent perovskite catalysts. Fresh

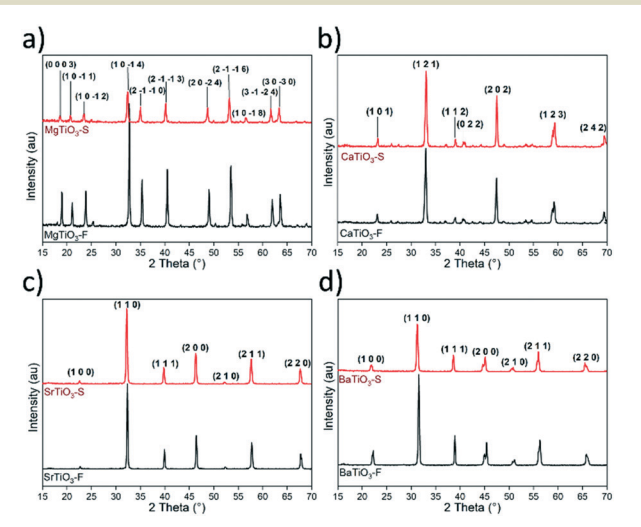


Fig. 3 Powder X-ray diffraction patterns of the studied perovskites: (a) MgTiO<sub>3</sub>, (b) SrTiO<sub>3</sub>, (c) CaTiO<sub>3</sub>, (d) BaTiO<sub>3</sub>. F, fresh perovskite catalyst; S, spent perovskite catalyst.

crystallizes in the hexagonal crystal system.<sup>54</sup> Fresh CaTiO<sub>3</sub> exhibited an orthorhombic habit. Both fresh SrTiO3 and BaTiO<sub>3</sub> samples crystallized in a cubic symmetry. The experimental XRD patterns are in agreement with previous reports.55-57

All the catalysts preserved their crystalline structure after plasma exposure, confirming their remarkable structural stability. Of all the studied catalysts, MgTiO3 is the only perovskite which shows a slight decrease in the relative intensity of XRD peaks when comparing the fresh vs. spent catalyst. This can be attributed (in part) to the known enhanced adsorption ability of Mg for NH3. FTIR on the spent perovskites was useful to explain this slight difference in XRD peak intensity for the fresh vs. spent Mg perovskite. We found that the intensity of the Ti-O-Ti asymmetric stretching<sup>58</sup> observed in all spent perovskite samples around 500 cm<sup>-1</sup> is lower for the spent Mg-based perovskite as compared to the other perovskites (Fig. S3†), which may correlate with the lower XRD intensity peak of this spent sample. The lower intensity of this stretching band suggests stronger interaction of Ti-O-Ti with ammonia. For instance, it has been demonstrated that among MgCl2, CaCl2, and BaCl<sub>2</sub> adsorbents confined on porous alumina, MgCl<sub>2</sub> salt had the highest total ammonia capacity in the 25-300 °C temperature range.59

Fig. 4 shows representative SEM images of the fresh and spent perovskite catalysts. Table S2† summarizes their average crystal sizes. The SEM images suggest no morphology change in all fresh and spent perovskite catalysts. Regarding the average crystal size, SrTiO3, CaTiO3, and BaTiO3 showed a slight increase in average crystal size for the spent catalysts as compared to the fresh catalysts. In the case of MgTiO3, an opposite trend was observed. The average crystal sizes were in the  $\sim$ 0.8–2.5 µm range and 0.9–2.2 µm range for the fresh and spent catalysts, respectively. Moreover, there is a reciprocal trend in the size of the crystal with the size of ion contained in the perovskite crystal lattice. For instance, Mg<sup>2+</sup>, the smallest ion of the group, ~145 pm, exhibited the largest perovskite crystals, while Ba<sup>2+</sup>, the largest ion of the group with an atomic radius of 253 pm, displayed the smallest crystals.

Since MgTiO<sub>3</sub> exhibited the best catalytic performance of all studied catalysts, we carried out additional experiments on this perovskite. Fig. 5 shows the ammonia synthesis rate vs. ammonia energy yield for MgTiO3 at the same 1:1 (N2:H2) ratio and 1:0.5:0.5 (N2:H2:He) ratio. The specific energy input (kJ L-1) for the three power values studied (5 W, 10 W and 20 W) are also delimited. We observed an increase in the intensity of all the nitrogen-activated plasma species, including  $H_{\infty}$ , when increasing the power from 5 W to 20 W, which correlates with the increase in ammonia synthesis rate increase from 5 W to 20 W (Fig. S4†). We chose the 1:1 ratio due to the better catalytic performance observed for this feed ratio as shown in Fig. 2. Moreover, under plasma environment limiting the amount of hydrogen with respect of the stoichiometic amount needed (i.e., N2:H2, 1:3) results beneficial. One should recall that it is easier to break the H2 than to activate

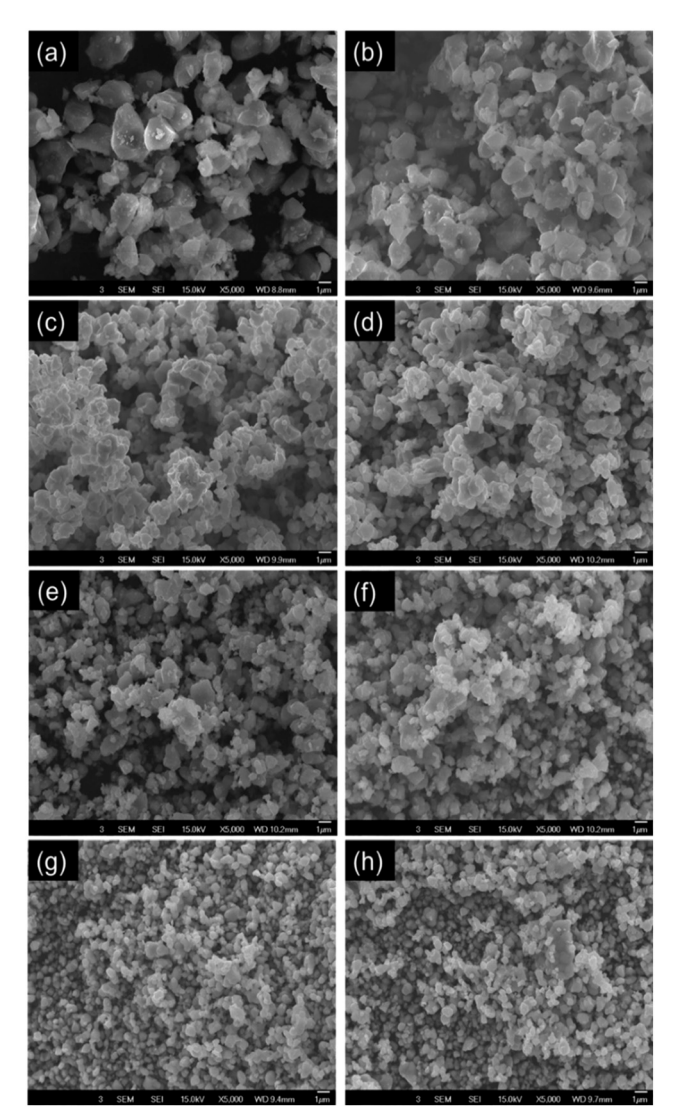


Fig. 4 Representative SEM images of the studied perovskites: (a)  $MgTiO_3$  fresh, (b)  $MgTiO_3$  spent, (c)  $SrTiO_3$  fresh, (d)  $SrTiO_3$  spent, (e)  $CaTiO_3$  fresh, (f)  $CaTiO_3$  spent, (g)  $BaTiO_3$  fresh, (h)  $BaTiO_3$  spent.

the triple nitrogen bond due to the energy required for each process. One of our central hypotheses  $^{21}$  is that an optimal catalyst for plasma-assisted ammonia synthesis is one that delays the recombination of adsorbed hydrogen radicals (H\*) into molecular hydrogen (H<sub>2</sub>), allowing them to instead bind to adsorbed nitrogen plasma activated species (N<sup>activated</sup>) to form NH\*. The possible excess of H atoms due to their easy production in plasma can favour the hydrogen recombination, which at the same time negatively impacts the main pathways for ammonia production. This can possibly explain the better performance observed at the 1:1 ratio.

#### The ammonia energy yield

Since we are employing an electron-based process, it is important to evaluate the energy employed. In this manuscript, the specific energy input (SEI) in kJ  $L^{-1}$  is

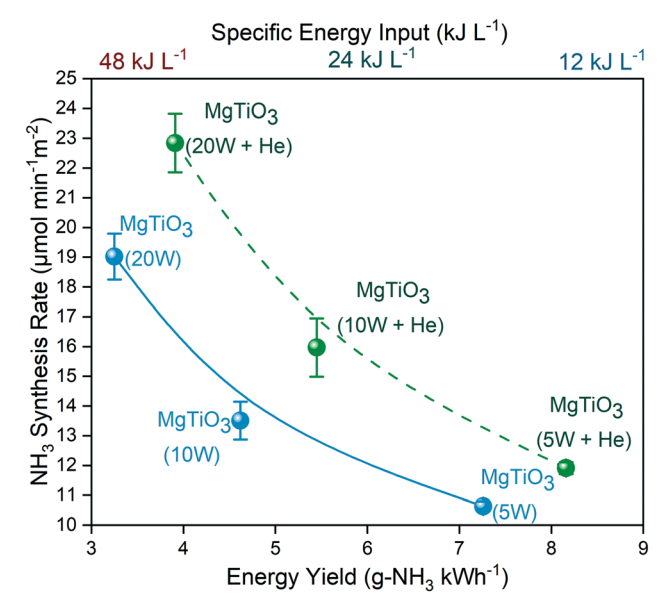


Fig. 5 Ammonia synthesis rate for MgTiO $_3$  at 1:1 (N $_2$ :H $_2$ ) and 1:0.5: 0.5 (N $_2$ :H $_2$ :He) flow ratio and total flow rate of 25 sccm at 5 W, 10 W and 20 W for MgTiO $_3$  perovskite.

defined as the measured power in kW divided by the input flow ratio to the reactor in liters per minute:

SEI (kJ 
$$L^{-1}$$
) = Power (kW)/Flow rate (L min<sup>-1</sup>) × (60 s/1 min)

From Fig. 5, it is clear that the lowest energy yield is obtained at the higher number of watts; however, the highest ammonia synthesis rate is observed at the highest power of 20 W. The highest synthesis rate for MgTiO $_3$  at 20 W was 22.84 µmol min $^{-1}$  m $^{-2}$  and 19.02 µmol min $^{-1}$  m $^{-2}$  with and without He, respectively, while the highest energy efficiency was observed for the 5 W experiment, being 8.16 g-NH $_3$  kW h $^{-1}$  and 7.26 g-NH $_3$  kW h $^{-1}$  for MgTiO $_3$  with and without He, respectively (the formulas employed for ammonia synthesis rate and energy yield can be found in the ESI† eqn. S1 and S2).

As already mentioned, some of the catalytic experiments were carried out in the presence of He. The main motivation for using He are the previous reports showing that the addition of He in a glow discharge plasma (0–8%) enhances the ammonia formation up to 45%. The effect of He has been explained by the increase in the electron temperature  $T_{\rm e}$ .

To determine the benefit of He without the perovskite in the chamber we also ran the plasma-only reaction with and without He. Details for the plasma-only reaction with and without He are shown in Fig. S5.† As can be seen in Fig. S5.† the addition of He results in the increase of ammonia production when using different feed ratios. Interestingly, when diluting the 1:1 ( $N_2:H_2$ ) mixture to 1:0.5:0.5 ( $N_2:H_2:H_2$ ) and the 1:3 ( $N_2:H_2$ ) mixture to 1:1.5:1.5 ( $N_2:H_2:H_2$ ), it is evident that the hydrogen content is limited. The limited hydrogen content might have a positive impact on the ammonia production due to its direct effect on the hydrogen recombination reaction as demonstrated by our group for

this reaction. 21,22 Moreover, we collected the OES for plasma + MgTiO<sub>3</sub> with and without He dilution, where we were able to observe a slight increase only in the intensity of the N2 (337.1 nm) plasma-activated species in the presence of He at 20 W. While the increase is small, one should recall that the He dilution was kept to a minimum (Fig. S6†).

#### The frequency effect on the ammonia production

To determine the frequency effect on the ammonia synthesis, we conducted experiments at a 1:1 (N2:H2) ratio at a total flow rate of 25 sccm while maintaining a constant applied voltage of 10 kV and having 0.1 grams of MgTiO3 packed in the reaction chamber (Fig. 6). From this figure, the ammonia production (synthesis rate) reaches a maximum at the frequency of 21 kHz with a value of 12.59 µmol min<sup>-1</sup> m<sup>-2</sup>, whereas the ammonia synthesis efficiency, i.e., energy yield, reaches the highest value of 4.56 g-NH<sub>3</sub> kW h<sup>-1</sup> at the frequency of 27 kHz. At higher frequency there is a possibility of increasing the synthesis efficiency due to the resonance effect of the dielectric barrier discharge that can contribute to the homogeneity of the discharge.<sup>62</sup>

#### Ammonia decomposition: the power effect

The high-power (20 W) experiments display the highest ammonia production synthesis rates. Nevertheless, while this high power can help the production of plasma-excited nitrogen species, it can also lead to detrimental plasmagenerated processes, such as an enhanced ammonia decomposition rate. This inference agrees with the lower electron impact dissociation energy for H2 and NH3 compared to N2, 4.5 eV for hydrogen<sup>63</sup> and 9.8 eV for nitrogen,63 while the N-H bond dissociation energy of NH3 is 4.67 eV with the following possible routes:<sup>64</sup>

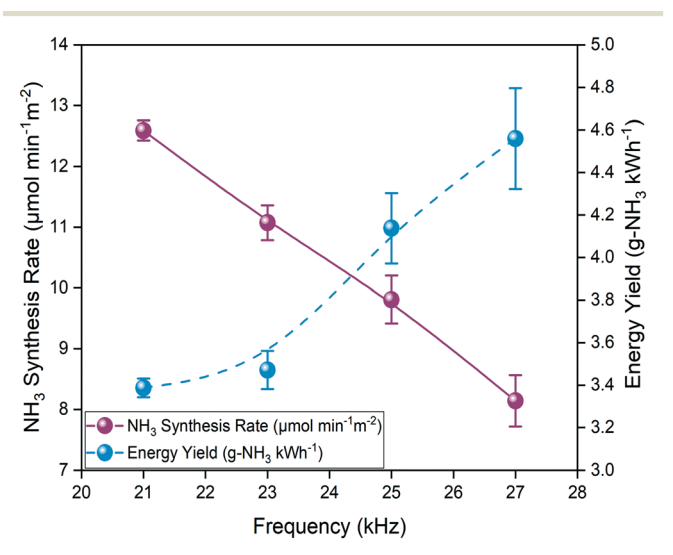


Fig. 6 Effect of the applied frequency on the ammonia synthesis rate and the energy yield for MgTiO3.

$$NH_3 \rightarrow NH_2 + H$$
,  $\Delta H = 4.67 \text{ eV}$ 

$$NH_3 \rightarrow NH + H_2$$
,  $\Delta H = 4.38 \text{ eV}$ 

$$NH_3 \rightarrow N + H_2 + H_1 + \Delta H = 7.63 \text{ eV}$$

To follow the ammonia decomposition as a function of the plasma power, we performed reactions at a total flow rate of 25 sccm at a ratio of 40:1 (N2:NH3) for safety and at a constant power of 5 W, 10 W and 20 W. It should be noted at this point by the reader that the ammonia production and decomposition concentrations are not within the same range, preventing us to make a direct net plasma ammonia synthesis vs. decomposition comparison. The ammonia decomposition yield can be expressed as:65

$$\mathrm{DY_{NH_3}} = \left(\frac{M_{\mathrm{NH_3}}(\mathrm{in}) - M_{\mathrm{NH_3}}(\mathrm{out})}{M_{\mathrm{NH_3}}(\mathrm{in})}\right) \times 100(\%)$$

where M represents the sccm of ammonia. From Fig. 7 it can be observed that ammonia decomposition increases as the number of watts increases. OES analysis shows that the peak intensity of the nitrogen-activated species is higher for a higher number of watts, which confirms the ability of the plasma to weaken the triple nitrogen bond and its capability of breaking the ammonia formed (Fig. S7†). The highest ammonia decomposition yield was 44.37% at 20 W corresponding to an energy yield of 5.06 g-NH<sub>3</sub> kW h<sup>-1</sup>. The importance of these results resides in the understanding of the reaction to improve the current catalyst and reactor design. The need of process intensification is evident where the produced ammonia can be adsorbed to prevent future electron collision and decomposition. This would allow

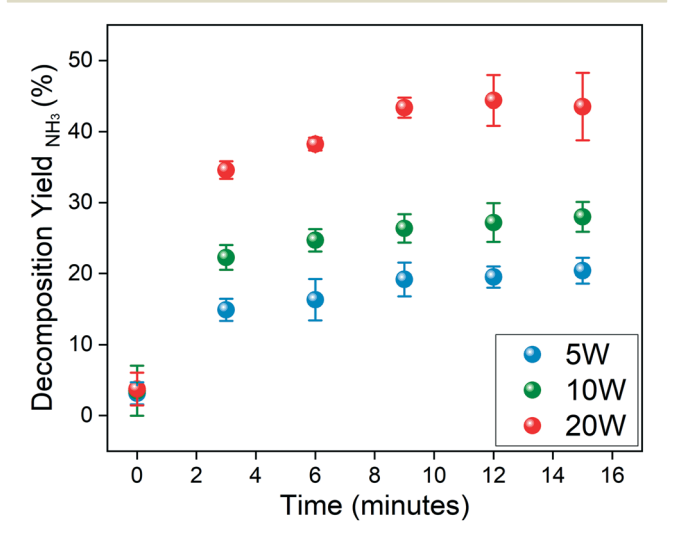


Fig. 7 Ammonia decomposition yield as a function of time for different applied powers for MgTiO<sub>3</sub> perovskite.

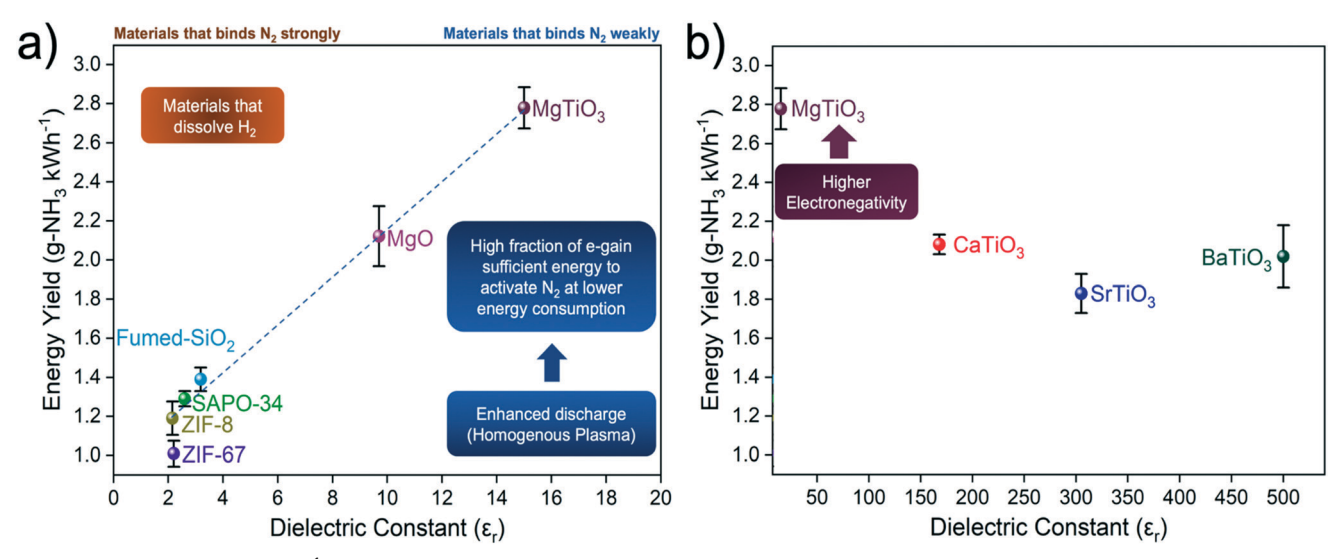


Fig. 8 Energy yield (g-NH<sub>3</sub> kW h<sup>-1</sup>) vs. dielectric constant (ε<sub>r</sub>) (a) for ZIF-67, ZIF-8, SAPO-34, fumed SiO<sub>2</sub>, MgTiO<sub>3</sub> and (b) for perovskites (xTiO<sub>3</sub>) employed in the study (x = Mg, Ca, Sr, Ba).

highly competitive ammonia synthesis rates, a prospect that can be potentially achieved with a plasma membrane reactor.

#### Comparison with other catalysts at similar plasma reaction conditions

Finally, to compare the performance of the best-performing perovskite, in this case MgTiO3, with other common materials employed in plasma catalytic ammonia synthesis such as zeolites (SAPO-34), MOFs (ZIF-67) and oxides, we performed the ammonia reaction at similar conditions when employing different materials as catalysts for ammonia synthesis. In Fig. 8, the experimental data collected at a 1:3 N<sub>2</sub>: H<sub>2</sub> ratio supports our central hypothesis related to the dielectric constant. Our hypothesis postulates that materials that have high dielectric constants such as perovskites can lead to an enhancement of the plasma discharge or homogeneous plasma.<sup>21,22</sup> The plasma homogeneity induced by the presence of perovskite can result in a higher probability of having electrons with the energy necessary to activate the N2 molecule. Therefore, a reduction in the required energy might be achieved as the power directed for reactant activation might be employed more efficiently, since plasma-awakened material properties might be exploited. Then, if the material intrinsic properties, such as hydrogen solubility and surface N2 binding energies (studied by our group previously<sup>21,22,26</sup>), can be merged dynamically, in principle the ammonia production can be boosted by orders of magnitude. In this case, MgTiO<sub>3</sub> contains the element with the highest electronegativity value of the group IIA elements, Mg, which helps in the dissociation of the triple nitrogen covalent bond, while the value of the dielectric constant for Mg perovskite leads to a greater homogeneity of the plasma. The synergy of both properties resulted in the observed ammonia production for this group IIA perovskite. Values for dielectric constants are shown in Fig. 8 for ZIF-67,66 ZIF-8,66

SAPO-34,<sup>67</sup> fumed silica,<sup>68</sup> MgO,<sup>69</sup> MgTiO<sub>3</sub>,<sup>70,71</sup> CaTiO<sub>3</sub>,<sup>72</sup> SrTiO<sub>3</sub>,<sup>72</sup> and BaTiO<sub>3</sub>.<sup>73</sup> When comparing with the available literature, the ammonia energy yield is enhanced when employing perovskites and a continuous plasma discharge was achieved (see Fig. S8 and Table S3†).

the best-performing perovskite, MgTiO<sub>3</sub> Clearly outperforms conventional porous materials. Specifically, ammonia production over the Mg-based perovskite is almost double the performance of traditional oxides, such as silica. These results confirm our key hypothesis on the importance of the dielectric constant and the use of perovskites as promising catalysts for plasma ammonia synthesis.

# Conclusions

In summary, we demonstrate that MgTiO<sub>3</sub> perovskite, which contains the most electronegative alkaline metal of all studied perovskites, leads to the highest ammonia synthesis rate. The high electronegativity of Mg assists in the dissociation of the triple nitrogen covalent bond. This intrinsic property of Mg perovskite together with the homogeneity of the plasma induced by the dielectric constant value of this perovskite is responsible for the high observed ammonia synthesis rate. The ammonia production over the Mg-based perovskite is almost double the performance of traditional oxides, such as silica, and some microporous crystals. By exploring the ammonia decomposition reaction, we observed an increase of the ammonia decomposition with plasma power increase. The highest ammonia decomposition yield was 44.37% at 20 W corresponding to an energy yield of 5.06 g-NH<sub>3</sub> kW h<sup>-1</sup>. This points out the benefit of running at low plasma power and the need to design plasma reactors where the newly formed ammonia molecules can be removed from the reaction system to avoid further electron collision, a perspective that can be achieved through intensification by the use of a plasma membrane reactor.

# Experimental setup

The catalytic activity was studied in a custom-designed dielectric barrier discharge (DBD) setup. The setup comprises four parts - the reactor core, emission spectrum capture setup, electrical characterization setup, and the gas chromatograph (GC) - to follow the catalytic activity. The complete setup is reported elsewhere.24 The reactor core comprises the reactor chamber only. To perform catalytic tests, nitrogen and hydrogen gases were fed to the reactor using mass flow controllers. The gases exiting the reactor are sent directly to the GC. The quantification was performed using an Agilent 7820A GC equipped with an HP-PLOTU column (30 m  $\times$  0.32 mm  $\times$  10  $\mu$ m) and a TCD detector and with hydrogen gas as carrier. The gases were bubbled in deionized water to ensure that all ammonia is captured and perform titration as an alternative method quantification. The high voltage power supply was connected to the reactor using Litz wire and alligator clips. The inner electrode is made of a tungsten rod (2.4 mm diameter) and is placed at the center of the quartz tube with an I.D. of 4 mm and O.D. of 6.40 mm. The fittings are chosen to be made of perfluoroalkoxy (PFA) to avoid any arc formation. The outer electrode is made of tinned copper mesh and acts as the ground electrode. The length of the plasma zone is approximately 7 cm. The impedance of the chamber was matched to deliver maximum power. The gases flow through the annulus and two quartz frits are placed carefully such that they do not cause any pressure increase. 100 mg of catalyst was loaded as a fine powder in the reactor. The reactor was purged with a mixture of nitrogen and hydrogen to remove oxygen after the reactor was sealed. The plasmacatalyst intersection zone is only 5 cm long. The catalyst was packed in the overlap area between the inner and the outer electrodes. The reactions were carried out at different N2 and H<sub>2</sub> feed flow ratios with a total flow rate of 25 sccm at a constant frequency of 25 kHz and average applied voltage  $V_{\rm pk-pk}$  of 12.5 kV  $\pm$  2.6 kV (see Lissajous plot and calculations in the ESI† file, Fig. S9a and b). The average bulk temperature of the reactor was measured to be approximately 171.7 °C ( $\pm$  4.9 °C). It is important to mention that in this work we did not control the temperature in any way or introduce any cooling means. To determine the ammonia synthesis rate, the exhaust gas was sent to the gas chromatograph calibrated for ammonia synthesis. The calibration curve details are provided in Fig. S10 and Table S4.† The reactor was connected to an oscilloscope to obtain the current and voltage waveforms. A Tektronix 2048 series oscilloscope was used along with a Tektronix P6015A highvoltage probe having a 1000× voltage reducing rating. The current was measured using a 10× current reducing probe to obtain the waveforms. The energy delivered to the reactor was calculated based on these measurements. Details on ammonia quantification reports are presented in Fig. S11.†

The light emitted from the discharge was led through an optical system and the emission spectra of the glow region were measured at the center of the tube. The measurements were recorded using a dual-channel UV-vis-NIR spectrophotometer in scope mode (Avantes Inc., USB2000 Series). The spectral range was from 200 to 1100 nm, using a line grating of 600 lines per mm and resolution of 0.4 nm. A bifurcated 400 µm fiber optic cable was employed. A schematic diagram of the reactor setup is presented in Fig. S12.†

#### Catalysts

The studied catalysts were purchased from Alfa Aesar and ACROS Organics: MgTiO<sub>3</sub> (Alfa Aesar, 11398, magnesium titanium oxide, 99% (metal basis)), CaTiO<sub>3</sub> (Alfa Aesar, 11397, calcium titanium oxide, 99+% (metal basis)), SrTiO<sub>3</sub> (Alfa Aesar, 11399, strontium titanium oxide, 99+% (metal basis)) and BaTiO<sub>3</sub> (barium titanate(IV), 99%, ACROS Organics<sup>TM</sup>). Before evaluating their catalytic performance, all catalysts were pretreated via two different methods, thermal pretreatment at 200 °C in an oven overnight and hydrogen plasma pretreatment with H2 at a total flow rate of 20 sccm for 10 minutes at 8 kV pk-pk and constant frequency of 27 kHz.

#### Catalyst characterization

For surface area analysis, 200-500 mg of sample was loaded for analysis on an ASAP 2020 surface area and porosity analyzer. Prior to analysis, samples were degassed at 150 °C for 3 h under vacuum. Isotherms were collected at 77 K. The surface areas for the fresh and spent perovskites are shown in Table S5.† The textural properties of fresh and spent perovskite catalysts are presented in Tables S6 and S7,† respectively.

FE-SEM images were collected on a JEOL ISM-700F instrument with an accelerating voltage of 15 kV.

X-ray diffractograms for fresh and spent perovskite catalysts were collected on a Siemens Kristalloflex810 unit operated at 25 mA, 30 kV, and CuKα radiation.

A Summit FTIR spectrometer (Nicolet) with an Everest diamond ATR attachment (Nicolet) and DTG detector was used to collect the spectra for the as-received powders. A range of 400-4000 cm<sup>-1</sup> with a step size of 4 cm<sup>-1</sup> was collected for all samples.

#### Author contributions

Maria L. Carreon conceived the idea, directed the plasma catalytic synthesis experiments, and contributed to the writing of the manuscript. Fnu Gorky, Beth A. Blake and Shelby R. Guthrie performed the plasma catalytic experiments and collected the reaction data. Moises A. Carreon, Jolie M. Lucero, and James M. Crawford helped with the characterization of the materials and with the discussion of the manuscript.

# Conflicts of interest

The authors declare no competing financial interests.

# Acknowledgements

Maria L. Carreon thanks the National Science Foundation (CBET award # 1947303). Moises A. Carreon thanks the National Science Foundation (CBET award # 1705675).

# Notes and references

- 1 Y. Tanabe and Y. Nishibayashi, Coord. Chem. Rev., 2013, 257, 2551-2564.
- 2 R. R. Schrock, Proc. Natl. Acad. Sci. U. S. A., 2006, 103, 17087.
- 3 https://www.globaldata.com/industries-we-cover/oil-gas/.
- 4 J. W. Erisman, M. A. Sutton, J. Galloway, Z. Klimont and W. Winiwarter, Nat. Geosci., 2008, 1, 636.
- 5 R. Schlogl, History of the Fritz-Haber-Institut, Department of Inorganic Chemistry, Fritz-Haber-Institute of the MPG, Germany, 1991.
- 6 B. S. Patil, Plasma (catalyst) assisted nitrogen fixation: reactor development for nitric oxide and ammonia production, Doctoral thesis, Technische Universiteit Eindhoven, Eindhoven, 2017.
- 7 E. Neyts and A. Bogaerts, J. Phys. D: Appl. Phys., 2014, 47,
- 8 J. C. Whitehead, J. Phys. D: Appl. Phys., 2016, 49, 243001.
- 9 X. Tu and J. C. Whitehead, Int. J. Hydrogen Energy, 2014, 39, 9658-9669.
- 10 Y. Li, Z. Fan, J. Shi, Z. Liu and W. Shangguan, Chem. Eng. J., 2014, 241, 251-258.
- 11 A. Fridman, Plasma chemistry, Cambridge university press,
- 12 E. C. Neyts, K. Ostrikov, M. K. Sunkara and A. Bogaerts, Chem. Rev., 2015, 115, 13408-13446.
- 13 M. L. Carreon, Plasma Res. Express, 2019, 1, 043001.
- 14 M. L. Carreon, J. Phys. D: Appl. Phys., 2019, 52, 483001.
- 15 P. Barboun, P. Mehta, F. A. Herrera, D. B. Go, W. F. Schneider and J. C. Hicks, ACS Sustainable Chem. Eng., 2019, 7, 8621-8630.
- 16 P. Mehta, P. Barboun, F. A. Herrera, J. Kim, P. Rumbach, D. B. Go, J. C. Hicks and W. F. Schneider, Nat. Catal., 2018, 1, 269-275.
- 17 P. Mehta, P. M. Barboun, Y. Engelmann, D. B. Go, A. Bogaerts, W. F. Schneider and J. C. Hicks, ACS Catal., 2020, 10, 6726-6734.
- 18 K. H. R. Rouwenhorst, H.-H. Kim and L. Lefferts, ACS Sustainable Chem. Eng., 2019, 7, 17515-17522.
- 19 L. R. Winter, B. Ashford, J. Hong, A. B. Murphy and J. G. Chen, ACS Catal., 2020, 10, 14763-14774.
- 20 J. R. Shah, J. M. Harrison and M. L. Carreon, Catalysts, 2018, 8, 437.
- 21 J. Shah, W. Wang, A. Bogaerts and M. L. Carreon, ACS Appl. Energy Mater., 2018, 1, 4824-4839.
- 22 J. Shah, F. Gorky, P. Psarras, B. Seong, D. A. Gómez-Gualdrón and M. L. Carreon, ChemCatChem, 2020, 12, 1200-1211.
- 23 J. Shah, T. Wu, J. Lucero, M. A. Carreon and M. L. Carreon, ACS Sustainable Chem. Eng., 2018, 7, 377-383.
- 24 J. R. Shah, F. Gorky, J. Lucero, M. A. Carreon and M. L. Carreon, Ind. Eng. Chem. Res., 2020, 59, 5167-5176.

- 25 F. Gorky, M. A. Carreon and M. L. Carreon, IOP SciNotes, 2020, 1, 024801.
- 26 F. Gorky, A. Best, J. Jasinski, B. J. Allen, A. C. Alba-Rubio and M. L. Carreon, J. Catal., 2021, 393, 369-380.
- 27 M. A. Green, A. Ho-Baillie and H. J. Snaith, Nat. Photonics, 2014, 8, 506-514.
- 28 K. C. Kao, Dielectric phenomena in solids, Elsevier, 2004.
- 29 H. T. Yi, T. Choi, S. G. Choi, Y. S. Oh and S. W. Cheong, Adv. Mater., 2011, 23, 3403-3407.
- 30 C. H. Ahn, K. M. Rabe and J. M. Triscone, Science, 2004, 303, 488-491.
- 31 M. A. Khan, U. S. Bhansali and H. N. Alshareef, Org. Electron., 2011, 12, 2225-2229.
- 32 C. Wu, K. Chen, D. Y. Guo, S. L. Wang and P. G. Li, RSC Adv., 2018, 8, 2900-2905.
- 33 A. Navrotsky, Physics and chemistry of earth materials, Cambridge University Press, 1994.
- 34 K. L. Pan, G. T. Pan, S. Chong and M. B. Chang, J. Ind. Eng. Chem., 2017, 52, 108-120.
- 35 A. Ogata, N. Shintani, K. Mizuno, S. Kushiyama and T. Yamamoto, IEEE Trans. Ind. Appl., 1999, 35, 753-759.
- 36 W.-C. Chung, K.-L. Pan, H.-M. Lee and M.-B. Chang, Energy Fuels, 2014, 28, 7621-7631.
- 37 F. Holzer, U. Roland and F.-D. Kopinke, Appl. Catal., B, 2002, 38, 163-181.
- 38 U. Roland, F. Holzer and F. D. Kopinke, Appl. Catal., B, 2005, 58, 217-226.
- 39 F. Holzer, F. Kopinke and U. Roland, Plasma Chem. Plasma Process., 2005, 25, 595-611.
- 40 K. Hensel, S. Katsura and A. Mizuno, *IEEE Trans. Plasma Sci.*, 2005, 33, 574-575.
- 41 K. Hensel, V. Martišovitš, Z. Machala, M. Janda, M. Leštinský, P. Tardiveau and A. Mizuno, Plasma Processes Polym., 2007, 4, 682-693.
- 42 Y. M. Baikov and E. K. Shalkova, J. Solid State Chem., 1992, 97, 224-227.
- 43 Y. M. Baikov, W. Gunther, V. P. Gorelov, P. Colomban and R. Baddour-Hadjean, *Ionics*, 1998, 4, 347–354.
- 44 G. Mannino, A. Alberti, I. Deretzis, E. Smecca, S. Sanzaro, Y. Numata, T. Miyasaka and A. La Magna, J. Phys. Chem. C, 2017, 121, 7703-7710.
- 45 B. D. James, D. A. DeSantis and G. Saur, Hydrogen Production Pathways Cost Analysis (2013-2016), Strategic Analysis Inc., Arlington, VA (United States), 2016.
- 46 Y. Horiuchi, G. Kamei, M. Saito and M. Matsuoka, Chem. Lett., 2013, 42, 1282-1284.
- 47 Y. Wang, M. Craven, X. Yu, J. Ding, P. Bryant, J. Huang and X. Tu, ACS Catal., 2019, 9, 10780-10793.
- 48 K. Persson, https://materialsproject.org/materials/mp-3771/, (accessed January, 2021).
- 49 K. Persson, https://materialsproject.org/materials/mp-4019/, (accessed January, 2021).
- 50 K. Persson, https://materialsproject.org/materials/mp-5229/, (accessed January, 2021).
- 51 K. Persson, https://materialsproject.org/materials/mp-2998/, (accessed January, 2021).

- 52 https://www.creative-chemistry.org.uk/alevel/core-inorganic/ periodicity/trends3, (accessed December, 29, 2020).
- 53 F. Gorky, J. M. Lucero, J. M. Crawford, B. Blake, M. A. Carreon and M. L. Carreon, ACS Appl. Mater. Interfaces, 2021, 13(18), 21338-21348.
- 54 R. P. Liferovich and R. H. Mitchell, Can. Mineral., 2006, 44, 1099-1107.
- 55 A. Beran, E. Libowitzky and T. Armbruster, Can. Mineral., 1996, 34, 803-809.
- 56 V. M. Longo, M. D. G. S. Costa, A. Z. Simões, I. L. V. Rosa, C. O. P. Santos, J. Andrés, E. Longo and J. A. Varela, Phys. Chem. Chem. Phys., 2010, 12, 7566-7579.
- 57 R. Waesche, W. Denner and H. Schulz, Mater. Res. Bull., 1981, 16, 497-500.
- 58 G. Busca, R. Gianguido, A. José, M. Gallardo, E. Vicente Sanchez and P. Paolo, J. Chem. Soc., Faraday Trans., 1994, 90, 3181-3190.
- V. E. Sharonov and Y. I. Aristov, React. Kinet., Mech. Catal., 2005, 85, 183-188.
- 60 A. de Castro, D. Alegre and F. L. Tabarés, Nucl. Mater. Energy, 2017, 12, 399-404.
- 61 M. B. Yaala, D. F. Scherrer, A. Saeedi, L. Moser, K. Soni, R. Steiner, G. De Temmerman, M. Oberkofler, L. Marot and E. Meyer, Nucl. Fusion, 2019, 60, 016026.
- 62 A. Fridman, A. Chirokov and A. Gutsol, J. Phys. D: Appl. Phys., 2005, 38, R1.

- 63 J. Hong, S. Prawer and A. B. Murphy, ACS Sustainable Chem. Eng., 2018, 6(1), 15-31.
- 64 S. Kundu, V. S. Prabhudesai and E. Krishnakumar, Phys. Chem. Chem. Phys., 2017, 19, 25723-25733.
- 65 P. Navascués, J. M. Obrero-Pérez, J. Cotrino, A. N. R. González-Elipe and A. Gómez-Ramírez, ACS Sustainable Chem. Eng., 2020, 8, 14855-14866.
- 66 M. Krishtab, I. Stassen, T. Stassin, A. J. Cruz, O. O. Okudur, S. Armini, C. Wilson, S. De Gendt and R. Ameloot, Nat. Commun., 2019, 10, 1-9.
- 67 M. Rybicki and J. Sauer, Catal. Today, 2019, 323, 86-93.
- 68 J. Robertson, Eur. Phys. J.: Appl. Phys., 2004, 28, 265-291.
- 69 J. Hornak, P. Trnka, P. Kadlec, O. Michal, V. Mentlík, P. Šutta, G. M. Csányi and Z. Á. Tamus, Nanomaterials, 2018, 8, 381.
- 70 B. D. Lee, H. Y. Ki, S. K. Eung and H. K. Tae, Jpn. J. Appl. Phys., 2003, 42, 6158.
- 71 V. M. Ferreira and J. L. Baptista, Mater. Res. Bull., 1994, 29, 1017-1023.
- 72 V. V. Lemanov, A. V. Sotnikov, E. P. Smirnova, M. Weihnacht and R. Kunze, Solid State Commun., 1999, 110, 611-614.
- 73 B. H. Hoerman, G. M. Ford, L. D. Kaufmann and B. W. Wessels, Appl. Phys. Lett., 1998, 73, 2248-2250.